



## Tracking large tabular icebergs using the SeaWinds Ku-band microwave scatterometer

K.M. Stuart<sup>\*</sup>, D.G. Long<sup>\*\*</sup>

Microwave Earth Remote Sensing Laboratory, Brigham Young University, 459 CB, Provo, UT 84602, United States

### ARTICLE INFO

Available online 13 December 2010

**Keywords:**

SeaWinds  
Scatterometer  
Resolution enhancement  
Icebergs  
Sea ice  
NSF Antarctic cruise

### ABSTRACT

Knowledge of iceberg locations is important for safety reasons as well as for understanding many geophysical and biological processes. Originally designed to measure wind speed and direction over the ocean, SeaWinds is a microwave scatterometer that operates at 13.4 GHz (Ku-band) on the QuikSCAT satellite. Radar measurements from SeaWinds are collected and processed on a daily basis using resolution-enhancement techniques to produce daily radar images. Because icebergs scatter microwave energy more than sea ice and sea water, icebergs are detected as high-backscatter targets surrounded by lower-backscatter regions in daily SeaWinds images. As a result, iceberg positions are determined in real-time and a time-series of iceberg positions is maintained in an Antarctic iceberg database by Brigham Young University's Microwave Earth Remote Sensing (MERS) laboratory. Since SeaWinds operates independent of both solar illumination and cloud cover and has a large daily spatial coverage, this paper demonstrates that SeaWinds is an excellent platform to detect and track large tabular icebergs. These icebergs are generally larger than 5 km and are typically characterized as a rough ice plateau above the surrounding sea water or sea ice. The number of icebergs tracked in the MERS Antarctic iceberg database is found to be generally greater than the number of icebergs tracked by the National Ice Center. The movement patterns of all icebergs detected by SeaWinds are also analyzed and 90% of icebergs are found to travel a counter-clockwise path around Antarctica and accumulate in the Weddell and Scotia Seas. Iceberg detection and tracking is demonstrated via multiple case studies that highlight icebergs C-19a and A-22a using the MERS database and through real-time operational support of the 2005, 2008, and 2009 NSF Antarctic cruises. Iceberg positions are validated by using collocated high-resolution satellite imagery and by navigating the NSF ships to physically intercept several large tabular icebergs in the Weddell and Scotia Seas.

© 2010 Elsevier Ltd. All rights reserved.

### 1. Introduction

Knowledge of iceberg locations is important for safety reasons as well as for understanding many geophysical and biological processes. For instance, iceberg positions affect shipping lanes, outline ocean currents, and influence biological productivity. Observed physical and electromagnetic characteristics of icebergs are also useful in estimating local weather conditions. Because of the importance of modeling the effects of icebergs in these regards, frequent iceberg observations are needed.

The United States National Ice Center (NIC) plays a major role in tracking the location of Antarctic icebergs. Current NIC methods for tracking icebergs primarily involve using optical satellite imagery, augmented by synthetic aperture radar (SAR) and

scatterometer images. Optical sensors produce high-resolution images but are unable to penetrate cloud cover and are dependent on solar illumination. Despite the high-resolution inherent in optical and SAR images, the spatial coverage of these sensors is limited, frequently resulting in poor temporal resolution. As a result, the NIC updates iceberg positions around every 20 days. These updates detail iceberg name and location where the name begins with a letter corresponding to the quadrant where it was first detected, followed by an incremental number. As icebergs fragment, each fragment name is appended with a letter (NIC, 2010).

This paper documents the tracking procedure for large tabular icebergs using the SeaWinds scatterometer. The icebergs of interest are generally larger than 5 km and can be characterized as a rough ice plateau above the surrounding sea water or sea ice. Originally designed to measure surface winds over the ocean, SeaWinds is a microwave scatterometer that operates at 13.4 GHz (Ku-band) onboard the QuikSCAT spacecraft (Spencer et al., 1997; Spencer and Long, 2000). Because SeaWinds operates at microwave frequencies,

<sup>\*</sup> Principle author.

<sup>\*\*</sup> Corresponding author.

E-mail addresses: [stuart@mers.byu.edu](mailto:stuart@mers.byu.edu) (K.M. Stuart),  
[long@ee.byu.edu](mailto:long@ee.byu.edu) (D.G. Long).

its radar measurements penetrate cloud cover and are independent of external illumination. QuikSCAT's sun-synchronous orbit allows SeaWinds to completely observe the polar regions daily. Backscatter measurements over a 24-hour period are collected and image reconstruction techniques are used to produce daily backscatter images that are used in the iceberg detection process. In these images icebergs are detected as high-backscatter targets surrounded by lower-backscatter sea water or sea ice. Icebergs are tracked on a daily basis and cataloged as part of the Scatterometer Climate Record Pathfinder (SCP) project at Brigham Young University's (BYU) Microwave Earth Remote Sensing (MERS) Laboratory (SCP, 2010). The MERS Antarctic iceberg database contains daily positions of nearly all of the icebergs reported by the NIC from 1999 to 2009 in addition to over 250 additional icebergs. Where possible, iceberg names in the MERS database correspond to names issued by the NIC. Icebergs in the MERS database not reported in the NIC iceberg database are labeled as "UK" (unknown) with an incremental number. While SeaWinds images are relatively coarse (2–4 km) resolution compared to optical photos or SAR images, the frequent observations and visibility of icebergs within the SeaWinds images enable accurate daily tracking of large Antarctic icebergs.

The iceberg detection methodology has been expanded to operate in near-real-time (NRT). Its utility is demonstrated via our operational support for the 2005, 2008, and 2009 United States National Science Foundation (NSF) Antarctic cruises (Smith, 2011). In the following, the methodology is described, unique concerns associated with tracking icebergs in NRT are highlighted, and respective solutions and trade-offs are outlined. To facilitate close-proximity research of icebergs during the NSF cruises, scatterometer images were also used to map the sea-ice edge. The tracking and reporting of the sea-ice edge using SeaWinds measurements is also briefly explored.

In 2005, 2008, and 2009, the NSF funded three cruises to travel to the Scotia and Weddell Seas to observe and record data related to iceberg characteristics and the impact of icebergs on nearby pelagic communities (Smith, 2011). To help direct ships to the dynamic positions of icebergs, the MERS Laboratory at BYU provided daily iceberg position updates to these cruises. The three case studies presented here demonstrate the ability and accuracy of using SeaWinds data to track icebergs in a near-real-time (NRT) environment. SeaWinds is the preferred instrument in this case because of its insensitivity to cloud cover and external lighting conditions and because extensive spatial and temporal coverage enables daily position updates. In the following, each cruise is considered. Concerns associated with tracking icebergs in NRT with SeaWinds data are highlighted, and respective solutions and trade-offs are outlined. Finally, the frequency of iceberg position reports during each cruise is indicated, and operations unique to each mission are reviewed.

## 2. Methods

To provide a framework for the iceberg detection process, the SeaWinds radar and corresponding measurements are briefly introduced. Radar measurements from SeaWinds are collected and processed using resolution-enhancement techniques to produce daily radar images with a sufficient resolution to track large tabular icebergs. To aid in interpreting these radar images, microwave scattering from common Antarctic scatterers is explored and microwave profiles for glacial ice, sea ice, and sea water are presented. Because glacial ice generally scatters microwave energy more than sea ice and sea water, icebergs are detected in daily SeaWinds images as high-backscatter targets surrounded by lower-backscatter sea ice and sea water.

### 2.1. SeaWinds radar

QuikSCAT was launched in 1999 to observe oceanic winds. Its orbit and wide swath enable near-complete coverage of the Earth's surface every 24 h. Daily coverage of the polar regions make it an ideal platform for high-latitude studies.

The primary instrument onboard QuikSCAT is the SeaWinds radar, a Ku-band scanning pencil-beam scatterometer. Scatterometers operate by transmitting a pulse of microwave energy towards the Earth's surface and measuring the reflected energy. In order to account for noise in each radar measurement, a separate measurement of the noise-only power is made and subtracted from the signal-and-noise measurement to determine the signal power. Given the signal-only power, the radar equation is used to calculate the normalized radar cross-section,  $\sigma^\circ$ , of the surface (Long and Spencer, 1997).

To collect backscatter measurements, the SeaWinds antenna rotates at 18 rpm and has two scanning conical beams, as illustrated in Fig. 1. The inner beam is horizontally polarized (h-pol) at a nominal incidence of 46°, and the outer beam is vertically polarized (v-pol) at a nominal incidence angle of 54° (Spencer et al., 1997). This design provides for four independent looks of the region lying within the inner swath and two independent looks of targets contained within the outer swath.

Each backscatter measurement represents the microwave return corresponding to an oval patch on the Earth's surface. Because of this shape, the backscatter values corresponding to these measurements are called "egg" backscatter values. SeaWinds uses onboard range-Doppler processing to separate each egg measurement into 12 subregions termed "slices" where each has a separate backscatter measurement (Spencer and Long, 2000). However, due to high error and noise levels in the outer-most slice measurements, usually only the inner eight slice measurements are used in processing (Early and Long, 2001; Spencer and Long, 2000). Because of the rapid roll-off of the aperture response function corresponding to each slice, individual response patterns are frequently represented as a binary mask corresponding to the 6 dB contour of each slice footprint, measuring approximately 6 × 25 km (Ashcraft and Long, 2003). Diagrams corresponding to the 6 dB contour of a single egg and associated eight slice antenna patterns are displayed in Fig. 2.

The measured backscatter value can be written as

$$\sigma^\circ = \frac{\int A(\tau)\sigma^\circ(\tau) d\tau}{\int A(\tau) d\tau} \quad (1)$$

where  $\sigma^\circ$  is a SeaWinds backscatter measurement,  $A(\tau)$  is the antenna gain of the 2-dimensional ground illumination footprint, and  $\sigma^\circ(\tau)$  is the spatial distribution of  $\sigma^\circ$  at the surface. The integrals are over the antenna footprint with respect to the 2-dimensional spatial index  $\tau$  (Long and Spencer, 1997).

### 2.2. Resolution enhancement

While individual  $\sigma^\circ$  measurements are useful in point-target analysis, it is desirable to generate backscatter images for macro-scale studies. A simple way to perform this task is a drop-in-the-bucket approach where measurements are binned by spatial location. This technique is termed "gridding" and produces gridded (GRD) images. Measurements from multiple passes are combined in image formation to provide sufficient coverage. The effective resolution of the resulting image is similar to the largest dimension of the spatial footprint (25 km), resulting in a coarse-resolution image (Spencer and Long, 2000). Alternately,  $\sigma^\circ$  measurements can be combined on a higher-resolution grid where values from each radar pulse are binned by spatial location and averaged by a

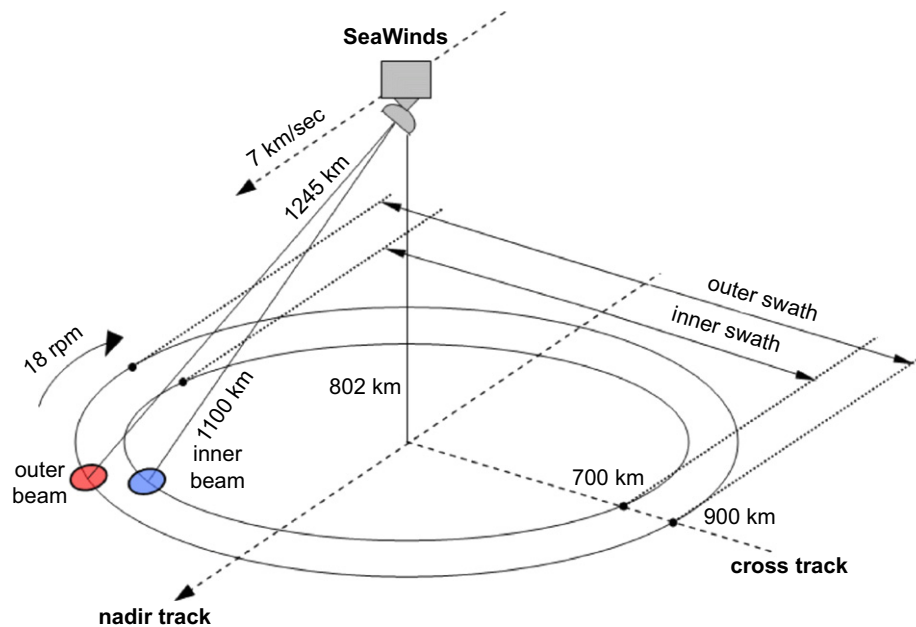


**Fig. 1.** An illustration of the SeaWinds observation geometry. SeaWinds has two scanning conical beams. The inner beam is horizontally polarized (h-pol) at a nominal incidence of  $46^\circ$ , and the outer beam is vertically polarized (v-pol) at a nominal incidence angle of  $54^\circ$ . This design provides for four different azimuth looks of the region lying within the inner swath and two azimuth looks of targets contained within the outer swath.

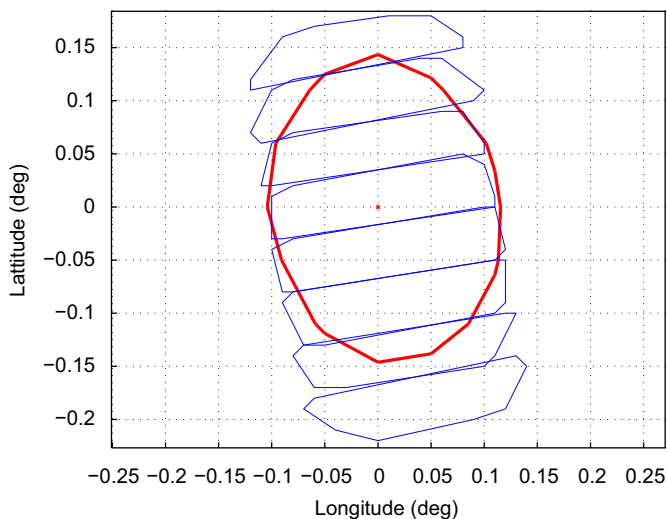


**Fig. 2.** An illustration of the 6 dB “egg” and “slice” antenna footprint on the Earth for a single SeaWinds backscatter egg measurement and associated slice measurements. The dark oval corresponds to the egg measurement and measures approximately  $35 \times 25$  km. The light contours represent slice measurement contours and measure approximately  $25 \times 6$  km.

weighting function where the weighting corresponds to the scatterometer spatial response function. This image technique is termed “AVE” (Long et al., 1993). While GRD and AVE images are effective in some large-scale studies, the dense sampling of SeaWinds measurements in the polar regions facilitates use of image reconstruction techniques to produce higher-resolution images (Spencer and Long, 2000).

The scatterometer image reconstruction (SIR) algorithm combines multiple backscatter measurements into a composite image with higher-spatial resolution than the associated aperture response via reconstruction techniques (Early and Long, 2001). SIR is an iterative multiplicative algebraic reconstruction technique

that combines overlapping measurements to produce a resolution-enhanced backscatter image. The SIR algorithm depends on dense, overlapping measurements which are assured by using radar measurements from multiple satellite passes. This results in a trade-off between spatial and temporal resolution. Daily SIR images produced from the egg dataset have a resolution of 8–10 km and are reported on a 4.45 km grid. Images reconstructed from slice measurements have a higher effective resolution of 4–5 km and are reported on a 2.225 km grid (Early and Long, 2001). Separate h-pol and v-pol images are created for each input type. For each case, the optimal number of iterations that minimizes the root-mean-squared error in simulation has been determined and is used to produce the SIR images. The GRD, AVE, and SIR images are produced as standard SeaWinds image data products (SCP, 2010).

The standard SeaWinds images used for the iceberg detection process are 24-hour slice-based h-pol SIR backscatter images. The temporal resolution of the images is set at 24 h to minimize noise in the reconstruction process yet provide for a short enough time segment to account for daily iceberg movement. In using 24-hour images, we assume there is generally negligible intra-day iceberg movement. SIR images are used to maximize the reconstructed spatial resolution, slice-based images are used because of their higher inherent spatial resolution, and h-pol backscatter images are used to maximize the backscatter contrast between common Antarctic scatterers, see Section 2.3. The differences between using h-pol and v-pol images are explored in Section 3.

Examples of standard SeaWinds h-pol backscatter images are displayed in Fig. 3, centered on South Georgia Island on Julian day (JD) 4, 2009. Egg-based and slice-based GRD, AVE, and SIR images are displayed for comparison in Fig. 3. In the center of each image is the high-backscatter signature of South Georgia Island, surrounded by low-backscatter sea water. Notice the greater spatial resolution inherent in the images derived from slice measurements. Also note the sharper contrast in backscatter around the perimeter of the island in the SIR images compared to AVE. For a more comprehensive outline and detailed explanation of the standard SeaWinds products, see SCP (2010). Trade-offs between using each image type in the iceberg detection process are discussed in Section 2.5.1.

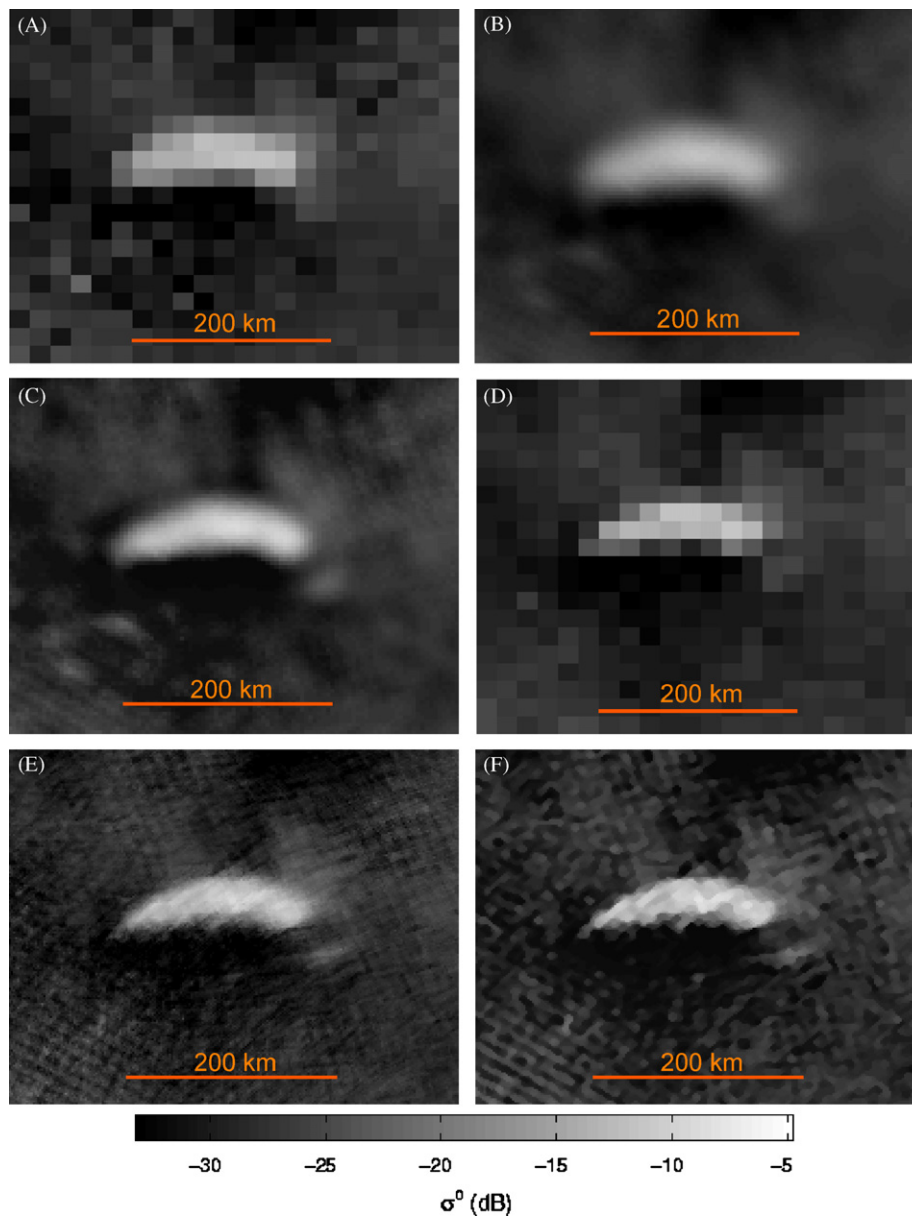


**Fig. 3.** Standard SeaWinds h-pol backscatter images of South Georgia Island for Julian day 4, 2009. Images differ by input data type (egg or slice) and processing method (GRD, AVE, or SIR). (A) Egg-based GRD image. (B) Egg-based AVE image. (C) Egg-based SIR image. (D) Slice-based GRD image. (E) Slice-based AVE image. (F) Slice-based SIR image. Pixel sizes correspond to 22.25, 4.45, and 2.225 km in the GRD, AVE, and SIR images. In the center of each image is the high-backscatter South Georgia Island, surrounded by low-backscatter sea water. Speckle in the low-backscatter regions is due to the temporal change and direction dependence in the wind-induced backscatter of the ocean, amplified by the reconstruction process.

### 2.3. Scattering theory

To interpret backscatter images in the polar regions, a brief explanation and comparison of the scattering properties of common Antarctic scatterers (sea water, sea ice, and glacial ice) is provided. Backscatter measurements collected by SeaWinds are the result of a combination of surface scatter and volume scatter. Surface scatter is the portion of energy reflected at the air-surface boundary. Volume scatter is the portion of energy transmitted into the snow and ice that reflect off internal particles. Both scattering components depend on the physical geometry and the dielectric of the material where the physical geometry characterizes both surface and internal parameters of the structure (Ulaby et al., 1981). The dielectric constant of sea ice and glacial ice is approximately unity except when moisture is present (Haykin et al., 1994).

Because sea water is a good conductor, all incident energy is reflected at the air-surface boundary, resulting in a dominant surface scattering component. The directivity of the reflected wave at the surface is governed by antenna geometry and sea surface roughness (Ulaby et al., 1981). Because SeaWinds transmits at an oblique angle with respect to the ocean's surface, the reflected pulse is generally directed away from the scatterometer, resulting in low  $\sigma^0$  measurements. The dominant surface feature affecting backscatter from sea water is the presence of wind (Long et al., 1996; Naderi et al., 1991). Near-surface winds induce capillary waves on the ocean's surface which roughen the ocean's surface, resulting in higher backscatter. The backscatter intensity is a function of wind speed, wind direction, and radar polarization. Sea water  $\sigma^0$  varies from  $-32$  to  $-15$  dB in daily SeaWinds images (see Section 2.4), depending on wind speed, with higher winds

resulting in higher  $\sigma^\circ$  (Long et al., 1996; Naderi et al., 1991; Sharma and D'Sa, 2008).

Backscatter from sea ice is dependent on surface and volume scattering and the sea ice concentration. Surface roughness is the dominant factor influencing surface scatter and is dependent on sea ice history. Sea ice history also defines the amount of volume scatter, e.g., multi-year sea ice is thicker and more compact, resulting in more internal particles reflecting incident radar energy and thus has a higher associated  $\sigma^\circ$  than thinner first-year sea ice (Massom, 1991; Zwally et al., 2002). Sea ice concentration is the percentage of the surface covered in sea ice, with higher sea ice concentrations resulting in generally higher  $\sigma^\circ$ . Sea ice has rough surface features and generally scatters more energy back to the radar than open water (Drinkwater et al., 2001). Sea-ice backscatter varies from  $-32$  to  $-5$  dB in daily SeaWinds images and is dependent on ice characteristics and water content (Forester et al., 2001).

Glacial ice is made of accumulated layers of snow which have a large particle size, dense crystalline structure, and a large penetration depth at microwave frequencies. The internal particles act as multiple reflectors, resulting in a dominant volume scattering component. Thus glacial ice tends to have a bright microwave return compared to both sea water and sea ice (Drinkwater et al., 2001). Glacial ice exhibits a  $\sigma^\circ$  of  $-25$  to  $-2$  dB in SeaWinds images.

It is important to note that the backscatter signatures from ice are dependent on weather. Liquid water due to melting drastically affects the dielectric constant of snow and ice, resulting in reduced  $\sigma^\circ$  during melting (Forester et al., 2001; Kunz and Long, 2004; Scambos et al., 2000). During the austral ablation, surface snow and ice on large tabular icebergs often melt, creating pools of freshwater. These pools are often extensive and are sometimes better characterized as lakes (Forester et al., 2001; Scambos et al., 2000, 2005). At microwave frequencies, these lakes lower the overall backscatter of the glacial ice, camouflaging it as open ocean. While generally undesirable, extreme melting conditions occasionally allow for a method of secondary iceberg detection. For example, if such an iceberg is surrounded by (i.e., encapsulated in) sea ice, there is frequently enough contrast between the low-backscatter surface water on the top of the iceberg and the medium-backscatter sea ice to identify the iceberg location. However, icebergs in open sea water that have significant surface water can be difficult to detect.

A sample backscatter image illustrating the  $\sigma^\circ$  returns from sea water, sea ice, and glacial ice is provided in Fig. 4. Land is characterized by high backscatter because of glacial ice covering the surface, sea ice has medium-backscatter values, and the lowest-backscatter regions correspond to sea water. The high-backscatter spots away from the continent correspond to icebergs and islands. Islands, being stationary at known locations, are readily distinguishable from icebergs. However, icebergs grounded on the ocean floor may appear as islands; this case is further explored in Section 2.5.1.

#### 2.4. Antarctic backscatter profiles

To characterize the radar backscatter from common Antarctic scatterers, Ku-band backscatter measurements of sea water, sea ice, and glacial ice below  $55^\circ\text{S}$  have been compiled from 1999 to 2009. To emphasize annual trends, backscatter values of all pixels of a given type are averaged by Julian day and compiled into histograms of daily backscatter values. The histograms are normalized in order to represent the overall backscatter probability distribution functions (PDFs). Fig. 5 illustrates the normalized average h-pol backscatter corresponding to sea water, sea ice,

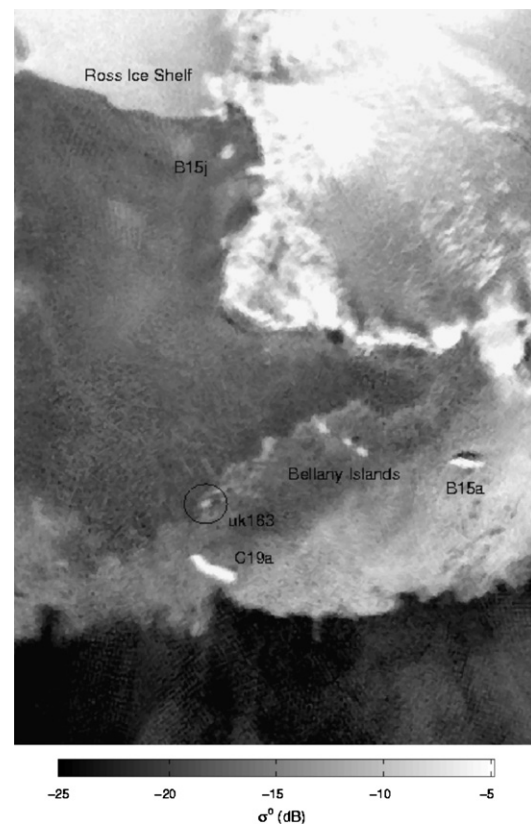


**Fig. 4.** H-pol backscatter image of the Ross Sea on 2007 Julian day 200. The highest-backscatter region corresponds to the Antarctic glacial continent which is surrounded by medium-backscatter sea ice. The lowest-backscatter regions correspond to sea water. The high-backscatter spots away from the glacial continent correspond to icebergs and islands.

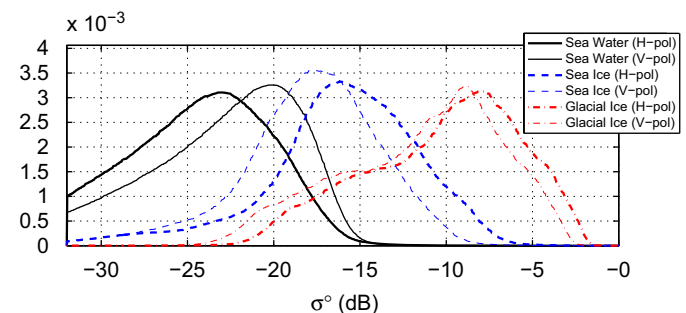


**Fig. 5.** Normalized backscatter histograms of sea water, sea ice, and glacial ice below  $55^\circ\text{S}$  on Julian day 1 from 1999 to 2009. Backscatter values from Julian day 1 of each year are averaged and subsequent values are normalized in order to estimate the backscatter probability distribution. Measurements are derived from standard daily slice-based SIR images.

and glacial ice for Julian day 1, years 1999–2009. This is near the peak of the melting season. Notice how the peaks of each medium are separately defined. Accurate classification of sea water, sea ice, and glacial ice depends on sufficient contrast between these PDFs.

As the daily backscatter PDFs in Fig. 5 are compiled for the entire Julian calendar, seasonal backscatter trends are observable. The h-pol and v-pol backscatter time-series for sea water, sea ice, and glacial ice for Julian days 1–365 are illustrated in Fig. 6. The statistical expectation of the PDFs in Fig. 6 are displayed in Fig. 7A, with the geometric mean and variance of the expected values presented in Table 1. Standard daily slice-based SIR images are used in this analysis.

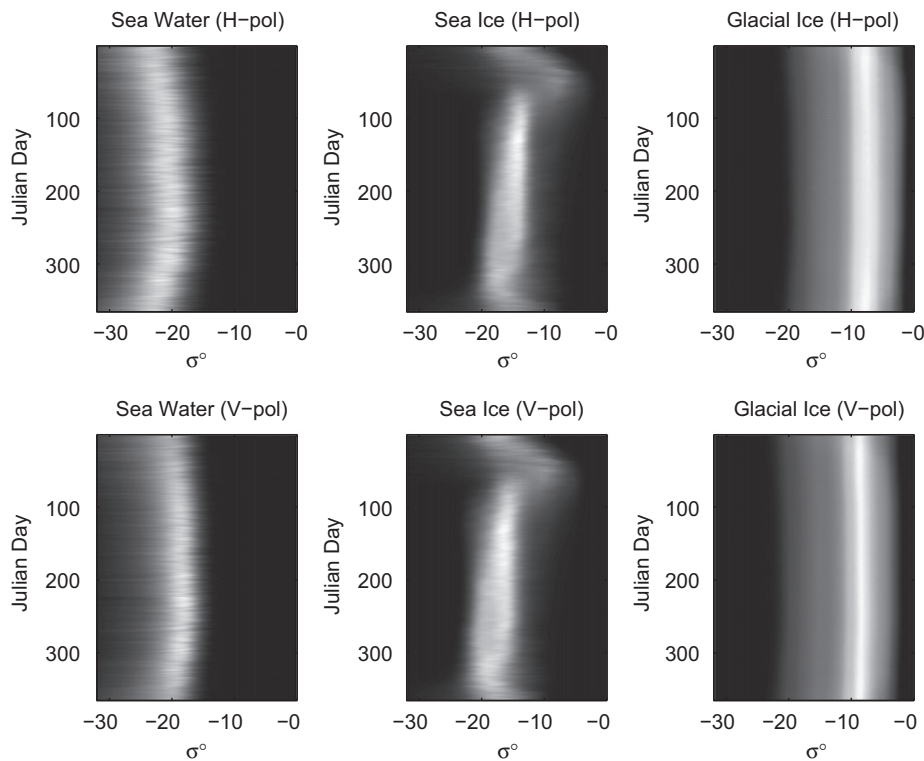


**Fig. 6.** Normalized histograms of SeaWinds h- and v-pol backscatter associated with sea water, sea ice, and glacial ice below 55°S from 1999 to 2009. Backscatter distributions for each Julian day are averaged and normalized in order to represent the time-varying backscatter PDFs of sea water, sea ice, and glacial ice. Backscatter values are derived from standard daily slice-based SIR images. Because each histogram is normalized, the intensity scale is arbitrary.

Seasonal trends in the backscatter PDFs are caused by variations in the electromagnetic and physical roughness of each medium (Ulaby et al., 1981; Haykin et al., 1994). Note that sea water backscatter is generally higher during the austral winter, peaking around Julian day 225. This trend is due to increased winds during the austral winter. We note that the average  $\sigma^0$  value of sea water is 0.6 dB higher at v-pol compared to h-pol.

Backscatter from sea ice is highest around Julian day 50, at the end of the austral summer. This is related to differences in overall sea ice area in the Southern Ocean, see Fig. 7B. Most of the 19 million km<sup>2</sup> of sea ice around Antarctica during the austral winter is first-year sea ice, while the majority of the 3 million km<sup>2</sup> of sea ice that survives the austral ablation is multi-year sea ice. The relatively-high backscatter detected during the austral summer, Julian day 1–100, corresponds to multi-year sea ice. The low-backscatter profile of the period from Julian day 100–150 is from both multi-year sea ice and newly-grown first-year sea ice that has a lower  $\sigma^0$ . Backscatter from Julian day 150–300 thus predominantly characterizes the 19 million km<sup>2</sup> of first-year sea ice. The period Julian day 300–350 characterizes the onset of the austral ablation and corresponds to first-year sea-ice recession. Average sea-ice returns are on average 2 dB higher at h-pol compared to v-pol. The average backscatter from glacial ice remains relatively constant throughout the year, with average h-pol measurements 1.2 dB higher than v-pol.

## 2.5. Iceberg detection

Scatterometer iceberg tracking exploits the backscatter differences between sea water, sea ice, and glacial ice to detect floating glacial ice fragments, i.e., icebergs. SeaWinds backscatter measurements are post-processed using the SIR algorithm and iceberg positions are manually determined from the daily images. In the following subsections, the methodology for detecting icebergs

from daily SIR images is outlined and alternative methods for tracking icebergs are also discussed. Concerns with tracking icebergs in near-real-time (NRT) are addressed, and respective solutions and trade-offs are presented. Finally, the format and frequency of iceberg position updates for the NSF Antarctic cruises are outlined.

### 2.5.1. Detection methodology

Icebergs are detected in daily SIR images as high-backscatter targets surrounded by lower-scattering sea water and sea ice, such as in Fig. 4. The estimated centroid of the high-backscatter targets are manually cataloged as the center of icebergs. Daily tracking takes advantage of previously observed iceberg positions. The tracking process is aided with knowledge of the common situations where icebergs are found and an understanding of iceberg movement patterns. The former is explored here and the latter is highlighted in Section 3.2.

Icebergs in the Antarctic calve from the terminus of glaciers or from ice sheets, potentially forming very large tabular icebergs (Bindschadler and Rignot, 2001; Kristensen, 1983). The largest observed iceberg was B15 at 10 838 km<sup>2</sup> (Ballantyne, 2002; Lazzara et al., 1999). Once broken away from a stationary glacier, icebergs fall under four basic categories: (1) free-floating icebergs free of sea ice, (2) grounded icebergs free from sea ice, (3) free-floating icebergs encapsulated in sea ice, and (4) grounded icebergs encapsulated in sea ice. Generally high contrast between icebergs and sea water make identification of icebergs an easy process. When icebergs are near the glacial continent in cases two and four, an established mask of the Antarctic glacial continent is helpful in differentiating between grounded icebergs and islands.

However, correctly detecting iceberg positions is difficult if the backscatter contrast between the iceberg and the background is insufficient. Backscatter contrast is reduced (1) when an iceberg is located in open water and high surface winds are present, (2) when

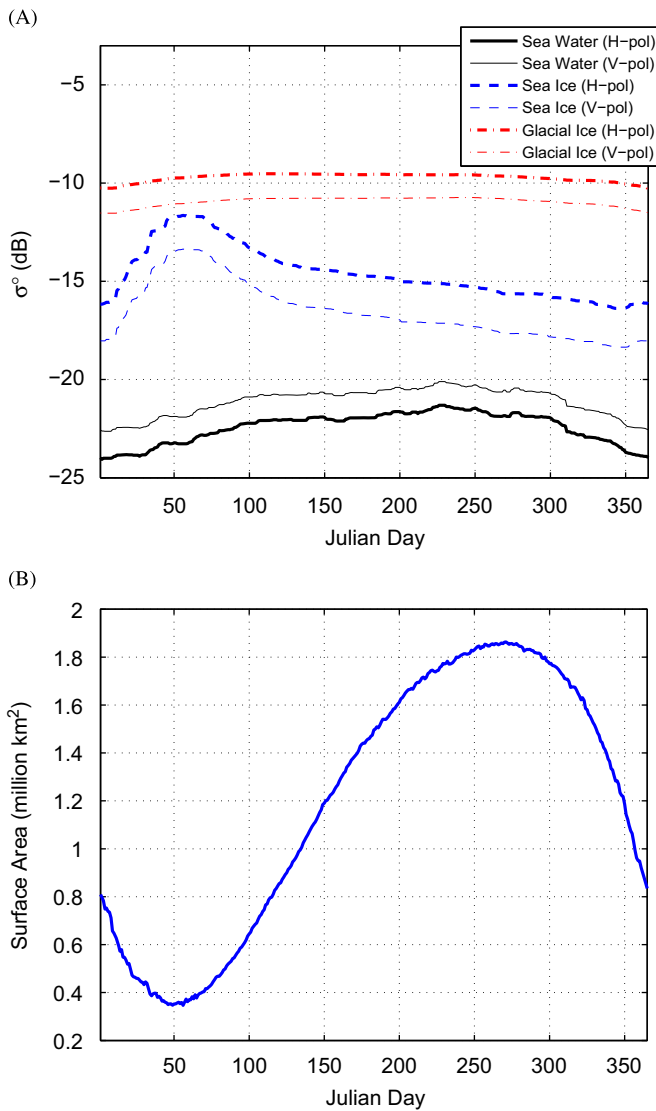


**Fig. 7.** (A) The statistical expectation of the backscatter PDFs in Fig 6 showing a time-series of the mean h and v-pol  $\sigma^0$  for sea water, sea ice, and glacial ice below 55°S from 1999 to 2009. Corresponding mean and variance parameters are contained in Table 1. (B) Average sea ice extent in the Southern Ocean from 1999 to 2009 as measured by the SeaWinds scatterometer.

**Table 1**

Geometric mean and variance of the expected backscatter return from sea water, sea ice, and glacial ice below 55° as measured by the SeaWinds scatterometer from 1999–2009.

Medium	Polarization	Mean (dB)	Variance (dB)
Sea water	H	-22.42	0.66
	V	-21.12	0.56
Sea ice	H	-14.58	1.86
	V	-16.53	2.08
Glacial ice	H	-9.71	0.04
	V	-10.93	0.05

an iceberg's surface experiences significant melting, (3) when an iceberg becomes too small (on the order of the image resolution), or (4) when an iceberg is in close proximity to land, ice, or other icebergs. The first two cases are discussed in Section 2.3. The third case is dependent on the resolution of SeaWinds images. The effective spatial resolution of the standard slice-based 24-hour SIR

products is 5–6 km. For an iceberg this size or smaller, the iceberg is frequently no longer discernible from its surroundings. Limited spatial resolution can also prevent accurate iceberg detection when icebergs are in close proximity to other glacial ice fragments. One location where this is common is “Iceberg Alley” in the Weddell Sea where icebergs occasionally collide or pass closely to other icebergs due to complex ocean currents (Macayeal et al., 2008; Ballantyne, 2002; Tournadre et al., 2008; Schodlok et al., 2006).

To ameliorate the difficulties of detecting icebergs in low-contrast environments and when icebergs pass closely, we use time-series animations of the daily backscatter images. These animations provide for a smooth framework to observe iceberg movement patterns, resulting in more complete iceberg tracks and reduced ambiguity. As a result, icebergs larger than 5 km can generally be tracked year-round on a daily basis (SCP, 2010).

While daily slice-based SIR images optimize spatial and temporal resolution in the iceberg detection process from SeaWinds data, it is appropriate to consider other image types: in particular, multi-day images. Multi-day SIR images are helpful when increased spatial resolution is desired at the expense of temporal resolution. With the inclusion of more measurements, noise is reduced and the resolution improved in the reconstruction process. As a result, stationary targets appear sharper in definition, while targets in motion may appear blurred.

AVE images may also be used to detect icebergs. As seen in Fig. 3E, the backscatter contrast in AVE images is more smoothed and is not as defined as in SIR images. However, AVE images are less computationally expensive than SIR images and have sufficient resolution to detect and track most large tabular icebergs (Early and Long, 2001). As a result, AVE images are frequently used in real-time tracking.

### 2.5.2. NRT iceberg tracking

The methodology for tracking icebergs previously outlined extends to tracking icebergs in NRT. However, there are three main concerns when tracking icebergs in a NRT environment. They are: accounting for the time difference between when backscatter measurements are recorded and when iceberg updates are received, updating the positions of existing icebergs, and accurately detecting and differentiating new icebergs from short-lived high-backscatter targets in the daily SIR images.

There is a variable delay between when SeaWinds radar measurements are collected and when iceberg positions are analyzed and then reported via email. Factors contributing to the time lag include the time required by SeaWinds to accumulate and down-link backscatter measurements, post-processing of radar measurements into SIR images, iceberg identification, and position up-link to the surface ship. While these functions may be streamlined to some extent, a minimum delay time frequently exists. During periods of rapid iceberg movement, this delay time may result in some discrepancy between reported and actual iceberg positions. As a result, it may be necessary to compensate for iceberg movement by predicting positions from past measurements and by observing nearby iceberg behavior.

In a NRT environment, previously tracked icebergs are not always distinguishable in current images from high-backscatter anomalies that may correspond to glacial ice fragments, multi-year sea-ice fragments, or other short-lived high-backscatter targets. Because accurate identification of new or resynchronization of lost icebergs may take several days, newly detected high-backscatter signatures are designated “TK” (temporary known) contacts. If these contacts survive and are confirmed in post-processing to be new icebergs, they are relabeled “UK” contacts. While “UK” contacts are included in the final MERS Antarctic iceberg database, “TK” contacts are not. Note that even though cruise logistics and

**Table 2**

Number of iceberg position reports provided for each NSF Antarctic cruise. Counts are divided into preliminary, interim, and post-mission updates. For an explanation of the temporal spacing of the iceberg reports, see the text.

Cruise	Pre-Mission	Interim	Post-Mission	Total
2005	14	31	7	52
2008	26	44	11	81
2009	15	40	2	57

sea-ice proximity limited the close-proximity research to only a select few icebergs, tracking all nearby contacts, including “TK” contacts, proved to be helpful in subjectively determining ocean current speed and direction for estimating future iceberg positions.

### 2.5.3. Cruise reports

For the three NSF cruises, updates which detailed the positions of local icebergs, the sea-ice edge, and other high-backscatter contacts were relayed to the ship. Daily updates were begun pre-mission to allow for efficient path planning, during the cruise to coordinate scientific efforts to locate moving icebergs, and post-mission for several weeks to allow for continued short-term scientific analysis. The number of updates provided during each cruise is detailed in Table 2. The variability in the number of updates provided per mission is addressed in each case study. To best support NRT operation, iceberg positions included in the iceberg updates were customized for each mission and are further highlighted in each respective mission report, see Section 3.4. The reports also included the location of sea ice and local wind conditions. All backscatter measurements have since been post-processed and iceberg positions have been updated from standard SIR images. These are available at (SCP, 2010).

## 3. Results

Using these iceberg detection techniques, the MERS Antarctic iceberg database details the position and backscatter of all large Antarctic icebergs detectable from SeaWinds measurements from 1999 to 2009. The iceberg database was updated periodically throughout the SeaWinds mission with icebergs added via post-processing and in NRT (SCP, 2010). With this database of iceberg positions, studies of iceberg characteristics are possible. For instance iceberg counts may be calculated and movement patterns may be examined. In the following sections, the count of icebergs from SeaWinds backscatter images from 1999 to 2009 is presented. Long-term movement patterns are presented and short-term movement patterns are highlighted via case study of iceberg C-19a. Finally, the ability and accuracy of using SeaWinds to track icebergs in NRT is demonstrated via support of the 2005, 2008, and 2009 NSF Antarctic cruises (Smith, 2011).

### 3.1. Iceberg counts

Fig. 8 presents the number of icebergs detected in SeaWinds backscatter images from 1999 to 2009 and the number of icebergs reported by the NIC during the same period. The NIC tracks icebergs larger than 10 nautical miles (nm) using optical sensors. The SeaWinds-derived iceberg database includes all of the NIC icebergs, plus additional icebergs visible in the SeaWinds images.

The annual fluctuations in the iceberg count at the peak of the austral ablation is due to melt conditions at the peak of the austral ablation. As noted previously, austral melting conditions decrease backscatter contrast between glacial ice, sea ice, and sea water, making iceberg detection more difficult and reducing the reported count. The iceberg count recovers after each ablation cycle for

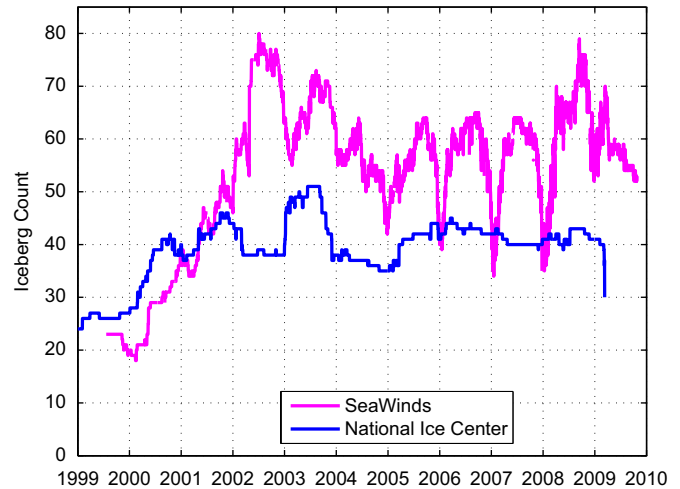


**Fig. 8.** Count of the number of Antarctic icebergs detected in daily SeaWinds backscatter images (gray) and reported by the NIC (solid) from 1999 to 2009. SeaWinds reports are daily; however, because the NIC reports iceberg positions periodically, the NIC iceberg count is an interpolated estimate, e.g., if the NIC reports positions for an iceberg on Julian days 10 and 250, this graph counts the iceberg over the entire interval.

icebergs that survive the summer melt cycle. The count is also increased by fragmentation of existing icebergs.

### 3.2. Iceberg movement

Because tabular icebergs have a deep draft and thus are deeply embedded in the ocean current, iceberg movement is typically dominated by oceanic currents (Guily, 1988). Near the coast of Antarctica, these currents sweep most icebergs in a counter-clockwise motion until they accumulate in the Weddell Sea, see Fig. 9. Icebergs are then propelled northward into the Scotia Sea along the “Iceberg Alley” corridor at approximately 50°W. Around 60°S, icebergs start moving in an eastward direction as they are swept into the Antarctic Circumpolar Current (ACC). By the time most icebergs reach the ACC, they have broken up; some however, survive for longer periods. As the size of fragments shrink, they become less detectable in the backscatter images (Stephen and Long, 2000; SCP, 2010; Scambos et al., 2005). The icebergs that do not follow this general pattern are pushed away from the glacial continent by katabatic winds while encapsulated in sea ice, and enter the ACC at other longitudes.

At the time of this publication, 90% of the icebergs contained in the MERS Antarctic iceberg database follow the general pattern described above. The 8% of icebergs are pushed away from the Antarctic continent by katabatic winds in the Ross Sea and drift into the southern Pacific Ocean. Approximately 2% of icebergs are pushed away from the glacial continent near the Davis Sea and float into the southern Indian Ocean. These patterns coincide with research performed in Tournadre et al. (2008).

### 3.3. Case study of iceberg C-19a

Sample iceberg detection tracking results are demonstrated in Fig. 10 for iceberg C-19a for Julian days 283–298 in 2008 when C-19a was in open water. This time-series illustrates changes in daily backscatter during the summer melt. Notice the gradual counter-clockwise rotation of iceberg C-19a over the time interval. Fig. 10F illustrates a negative consequence of using multiple passes to create SIR images. Since multiple satellite passes over a 24-hour period are used to create SIR images, very rapid changes in the iceberg orientation from pass to pass may cause an echo effect in

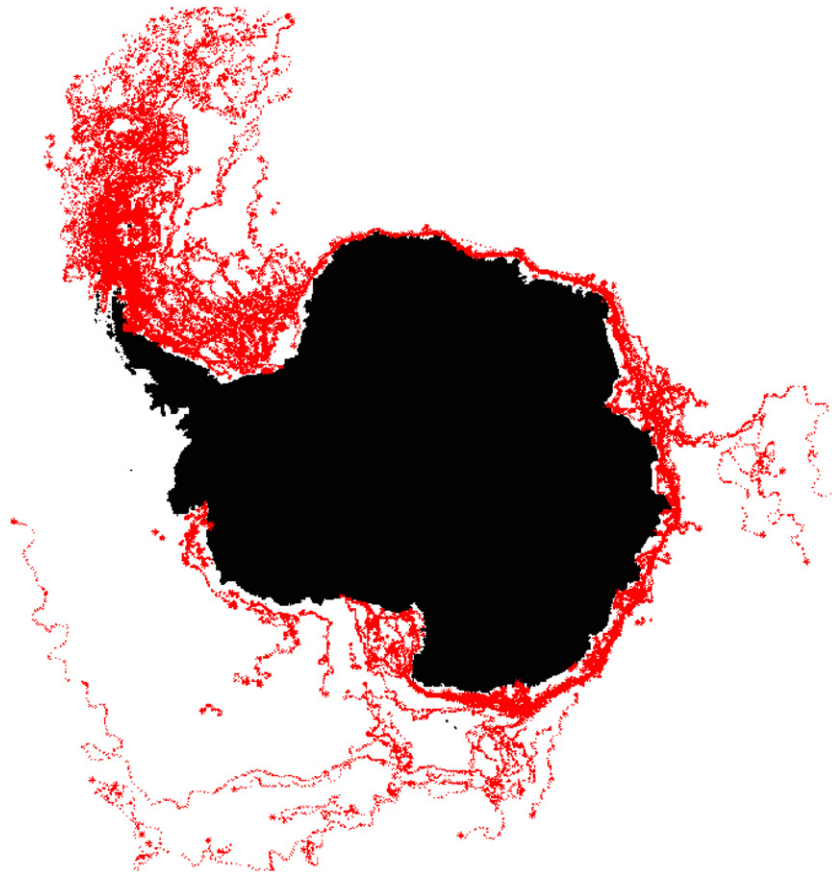


**Fig. 9.** A depiction of Antarctic icebergs detected by SeaWinds from 1999 to 2009. The majority of icebergs travel counter-clockwise around the perimeter of Antarctica and accumulate in the Weddell Sea. They are then propelled into the Scotia Sea along a northward corridor, frequently called “Iceberg Alley.” Upon reaching 60°S, icebergs are swept into the Antarctic Circumpolar Current (ACC). Icebergs that do not follow this general pattern are pushed away from the glacial continent by katabatic winds while encapsulated in sea ice, causing these icebergs to enter the ACC at other longitudes.

the daily SIR images. However, this is rare. Fig. 10K depicts a melt event on 2008 Julian day 291. Spanning over 100 km, one end of iceberg C-19a remains frozen and retains its high backscatter profile while the opposite end is likely undergoing surface melt. The increase in surface moisture results in decreased microwave penetration and thus a decrease in volume scatter. As a result, the backscatter from the left end of iceberg C-19a in Fig. 10K is diminished, resulting in reduced contrast compared to the surrounding sea water.

#### 3.4. NSF cruise case studies

The three case studies for cruises in 2005, 2008, and 2009 presented here demonstrate the ability and accuracy of using SeaWinds data to track icebergs in a NRT environment. SeaWinds is the preferred instrument in this case because of its insensitivity to cloud cover or lighting conditions and because extensive spatial and temporal coverage enables daily position updates. In the following, each cruise is considered and operations unique to each mission are reviewed.

##### 3.4.1. The 2005 cruise

The first NSF Antarctic cruise took place in 2005 from Julian day 331 to 361. This first cruise required the initial setup of NRT processing of SIR images for the region of intent. Once this process was developed, daily iceberg positions were extracted from the most recent SIR images and subsequently included in the daily reports. Corresponding SIR images with iceberg annotations were also included in the daily updates; however, due to up-link size

constraints, smaller custom SIR images were created. These custom backscatter images were bounded by 65°S, 55°S, 60°W, and 40°W. Images were manually annotated to indicate iceberg positions and sea-ice extent. General wind conditions were estimated based on sea-surface roughness observed in the backscatter images.

Throughout the cruise, a total of 15 icebergs were tracked in the Scotia and Weddell Seas. A summary of some of the lifetime and mission-specific statistics of icebergs and high-backscatter contacts during this time is included in Table 3, detailing detection dates, initial and final tracking positions, initial and final positions with respect to the cruise, average daily movement during the cruise, a flag indicating sea ice encapsulation during the cruise, and iceberg dimensions as reported by the NIC during the cruise. Iceberg tracks during the time of the cruise are illustrated in Fig. 11. Even though this cruise took place during the austral ablation, the outlying sea ice had yet to melt away from the south Scotia Sea; therefore, the majority of icebergs in the Weddell Sea were encapsulated in first-year sea ice during the cruise period. As a result, only iceberg A-52 was visited (twice) of the 15 icebergs tracked.

##### 3.4.2. The 2008 cruise

The second NSF Antarctic cruise took place in 2008 from Julian day 153 to 177. During this cruise, multiple icebergs were detected and tracked in the Scotia and northern Weddell Seas. Corresponding iceberg and “TK” contact information and statistics are presented in Table 4. Corresponding iceberg track illustrations are in Fig. 12. Many icebergs were located near the sea-ice edge. As a result of a late austral fall, exploration in the Weddell Sea was

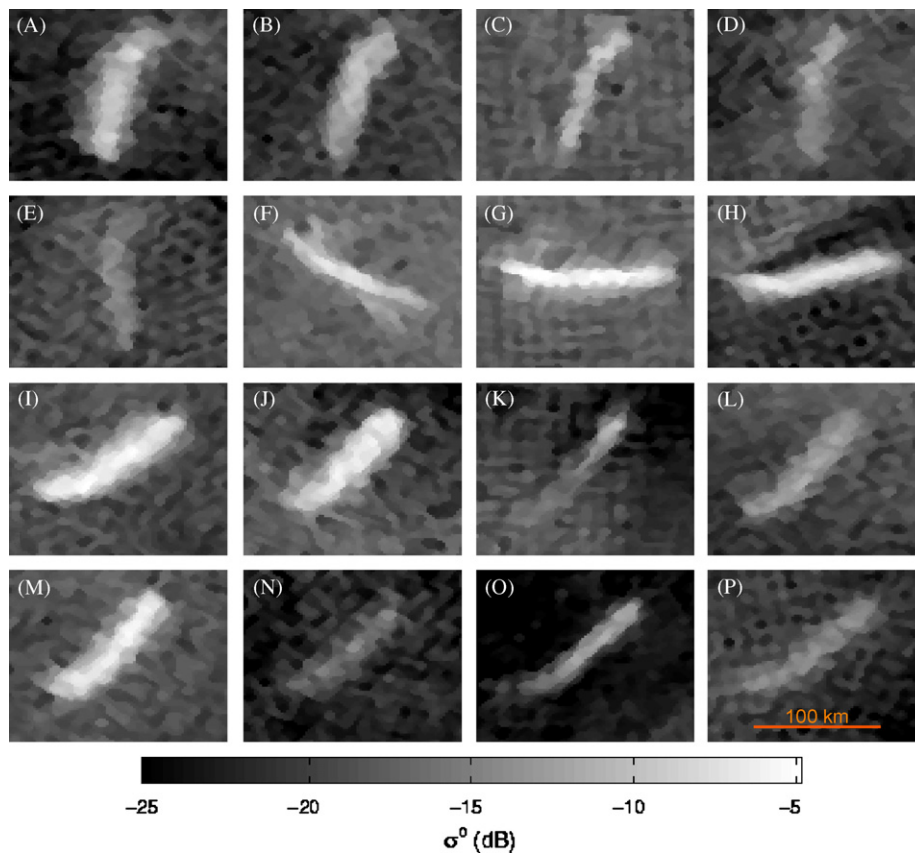


**Fig. 10.** SeaWinds h-pol backscatter time-series of iceberg C-19a for 2008, Julian days 283–298. Higher-backscatter values correspond to iceberg C-19a and lower-backscatter values correspond to sea water.

**Table 3**  
Compilation of icebergs and high-backscatter targets detected by the SeaWinds scatterometer in the Weddell and Scotia Seas during the 2005 NSF Antarctic cruise. Lifetime and mission-specific statistics are illustrated for each contact including detection dates, position, average daily movement during the cruise, a flag indicating sea ice encapsulation during the cruise, and iceberg dimensions reported by the NIC. See Fig. 11 for corresponding track illustration. Icebergs visited during the cruise are indicated with “\*”.

Lifetime information				Cruise-Specific information (2005 JD 331–361)				
Name	Track dates	Initial pos. (° N, ° E)	Final pos. (° N, ° E)	Initial pos. (° N, ° E)	Final pos. (° N, ° E)	Avg. daily movement (km)	Sea ice	NIC size (nm)
A-27	99JD200-09JD244	−76.23, −43.33	−74.84, −39.88	−76.26, −43.60	−76.26, −43.60	0.0	Y	10 × 8
A-22a	99JD202-07JD296	−76.36, −46.07	−48.63, −16.27	−65.40, −53.86	−64.23, −54.04	6.7	Y	36 × 27
A-23a	99JD202-09JD244	−76.27, −41.81	−76.05, −41.35	−76.15, −41.66	−76.15, −41.66	0.0	Y	46 × 43
A-43d	01JD123-09JD244	−71.20, −58.70	−70.52, −58.08	−71.30, −58.56	−71.30, −58.56	0.0	Y	27 × 18
A-43f	01JD157-09JD021	−71.63, −59.40	−50.77, −25.27	−66.59, −59.44	−66.52, −60.02	5.1	Y	29 × 17
A-52*	03JD063-06JD124	−65.69, −60.95	−54.70, −37.29	−61.13, −51.64	−60.69, −53.26	10.8	N	21 × 10
A-53a	05JD120-08JD116	−67.11, −60.24	−51.44, −33.25	−67.22, −60.25	−67.03, −60.04	0.8	Y	29 × 14
UK-138	05JD110-06JD261	−69.91, 6.40	−65.22, −54.16	−73.47, −38.48	−74.13, −44.70	4.4	Y	–
UK-139	05JD202-05JD365	−72.29, −23.35	−71.71, −43.44	−71.43, −36.53	−71.83, −43.54	9.8	Y	–
UK-140	05JD202-05JD355	−70.43, −20.50	−70.70, −30.64	−69.78, −28.11	−70.70, −30.64	8.1	Y	–
UK-206	04JD315-05JD348	−75.47, −35.61	−64.96, −40.54	−64.65, −40.22	−64.96, −40.54	9.9	Y	–
UK-207	04JD318-06JD275	−76.21, −40.03	−56.85, −36.38	−67.37, −47.73	−66.70, −49.52	5.3	Y	–
UK-210	04JD358-05JD359	−78.08, −43.90	−65.96, −52.93	−67.86, −51.02	−65.96, −52.93	12.4	Y	–
UK-215	05JD018-06JD306	−67.83, 33.64	−62.87, −41.40	−73.28, −27.87	−74.35, −33.49	7.6	Y	–
UK-221	05JD124-06JD022	−66.17, −59.57	−66.27, −60.78	−65.78, −58.86	−66.07, −59.85	1.6	Y	–

prevented because of advancing sea ice. Consequently, only iceberg A-43k and contacts UK-238 and UK-250 were visited. One iceberg (UK-238) was encapsulated in sea ice part of the time during the cruise. As a result, the sea-ice encapsulation flag for this iceberg is indicated as “M” (“Mixed”) in Table 4.

Similar to the 2005 cruise, daily updates included iceberg positions and custom SIR images. However, due to an increase in the number of accessible icebergs, there was a need for greater

temporal resolution. To meet this need, a specialized SIR product was implemented for NRT operation to enable iceberg position updates twice per day. The morning update was derived from multiple SIR images produced using the backscatter measurements collected from the previous 12 and 24 h. Compared to the 24-hour SIR images, the 12-hour SIR images have greater temporal resolution at the expense of reduced spatial resolution and reduced backscatter contrasts between sea water, sea ice, and glacial ice. If

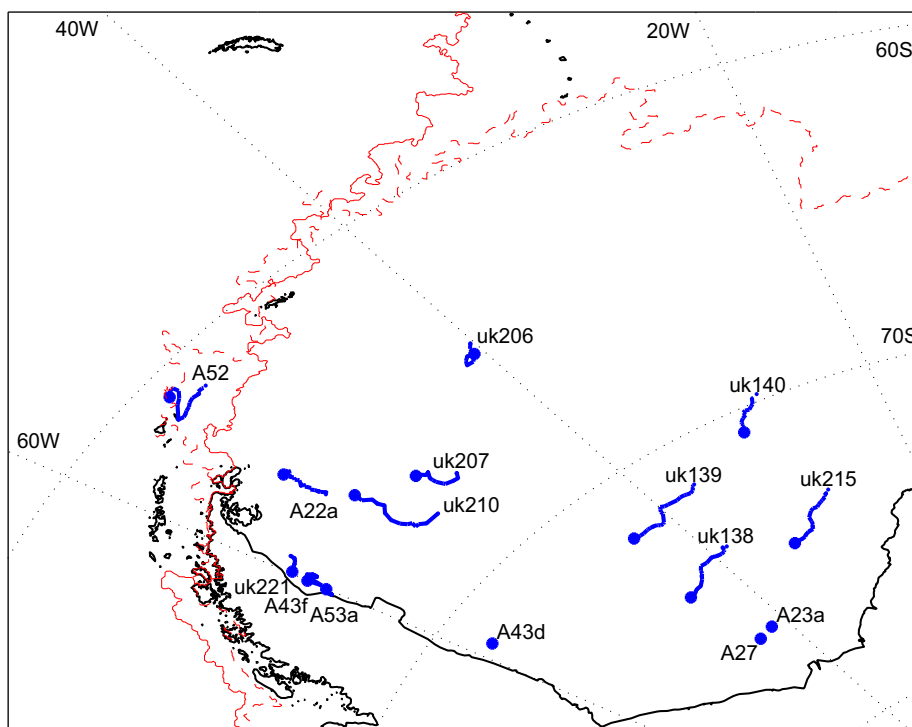


**Fig. 11.** Tracks of Antarctic icebergs and high-backscatter contacts detected using SeaWinds in the Weddell and Scotia Seas during the 2005 NSF Antarctica cruise. Final iceberg tracking positions are indicated with “\*”. The Antarctic peninsula and the Filchner–Ronne Ice Shelf are outlined at the bottom of the image. The sea-ice edge at the beginning and ending of the cruise is indicated by solid and dashed lines. See Table 3 for corresponding iceberg statistics.

**Table 4**

Compilation of icebergs and high-backscatter targets detected by the SeaWinds scatterometer in the Weddell and Scotia Seas during the 2008 NSF Antarctic cruise. Lifetime and mission-specific statistics are illustrated for each contact including detection dates, position, average daily movement during the cruise, a flag indicating sea ice encapsulation during the cruise, and iceberg dimensions reported by the NIC. See Fig. 12 for corresponding track illustration. Icebergs visited during the cruise are indicated with “\*”.

Lifetime information				Cruise-Specific information (2008 JD 153–177)				
Name	Track dates	Initial pos. (° N, ° E)	Final pos. (° N, ° E)	Initial pos. (° N, ° E)	Final pos. (° N, ° E)	Avg. daily movement (km)	Sea ice	NIC size (nm)
A-23a	99JD202-09JD244	–76.27, –41.81	–76.05, –41.35	–76.14, –41.59	–76.14, –41.59	0.0	Y	40 × 32
A-27	99JD200-09JD244	–76.23, –43.33	–74.84, –39.88	–75.15, –41.56	–75.15, –41.56	0.0	Y	10 × 8
A-43d	01JD123-09JD244	–71.20, –58.70	–70.52, –58.08	–71.29, –58.47	–71.29, –58.47	0.0	Y	21 × 15
A-43f	01JD157-09JD021	–71.63, –59.40	–50.77, –25.27	–56.44, –34.35	–52.89, –36.75	22.3	N	27 × 9
A-43k*	08JD003-09JD095	–62.37, –53.59	–51.55, –11.10	–57.77, –43.54	–58.01, –42.52	5.4	N	25 × 8
A-56	08JD148-09JD244	–77.12, –50.12	–77.15, –49.94	–77.14, –50.04	–77.15, –50.01	2.5	Y	14 × 7
A-57	08JD151-09JD145	–77.40, –48.24	–77.60, –47.59	–77.40, –48.05	–77.50, –47.90	4.0	Y	19 × 5
B-15d	00JD231-08JD330	–76.38, –179.02	–49.06, –37.51	–55.83, –43.67	–55.13, –42.81	11.2	N	25 × 5
B-15l	07JD054-09JD244	–66.48, 46.60	–62.06, –37.97	–71.47, –37.68	–70.58, –38.40	5.9	Y	16 × 7
C-8	99JD202-09JD244	–67.30, 147.08	–60.87, –43.21	–65.93, –55.67	–65.92, –55.42	0.6	Y	15 × 8
C-18a	05JD152-09JD244	–65.20, 115.25	–59.92, –45.05	–73.50, –47.17	–72.34, –47.63	6.3	Y	17 × 3
C-19d	03JD173-09JD244	–69.53, 163.30	–57.08, –49.17	–74.68, –35.88	–74.26, –38.63	6.0	Y	17 × 8
C-21a	05JD079-08JD208	–66.09, 90.27	–54.62, –40.61	–56.80, –46.83	–56.02, –45.01	11.1	N	10 × 8
D-18	06JD053-09JD028	–69.96, 8.92	–56.79, –17.88	–60.21, –39.18	–59.00, –39.88	7.0	Y	11 × 4
UK-148	06JD085-08JD288	–67.52, 44.39	–68.05, –36.69	–73.32, –40.19	–72.44, –41.27	5.7	Y	–
UK-157	07JD032-09JD244	–76.51, –46.70	–73.97, –42.52	–76.27, –46.58	–76.25, –46.74	0.7	Y	–
UK-177	07JD030-08JD330	–74.21, –32.59	–50.88, –32.97	–59.72, –44.15	–56.99, –39.00	14.9	N	–
UK-235	08JD019-08JD237	–63.63, –51.91	–55.57, –40.58	–57.59, –46.50	–59.47, –46.05	18.1	N	–
UK-238*	08JD090-08JD165	–60.74, –52.53	–60.40, –48.85	–60.63, –51.82	–60.40, –48.85	14.2	M	–
UK-246	08JD090-08JD200	–74.25, –27.93	–71.50, –39.32	–72.49, –38.03	–71.92, –38.55	6.2	Y	–
UK-247	08JD074-09JD103	–59.86, –47.90	–55.46, –35.52	–59.51, –46.72	–58.56, –43.97	16.6	N	–
UK-248	08JD102-08JD344	–58.61, –44.39	–51.93, –37.58	–56.87, –43.74	–55.27, –41.06	23.3	N	–
UK-250*	08JD131-08JD216	–61.97, –56.83	–59.80, –46.86	–60.51, –55.88	–59.43, –52.72	16.6	N	–

sufficient contrast existed in the 12-hour SIR images, iceberg positions were extracted. If not, 24-hour SIR images were used. This process was repeated in the evening.

Upon post-mission review, it was found that while 12-hour SIR images provided greater temporal resolution, spatial resolution and image contrast were frequently too degraded to

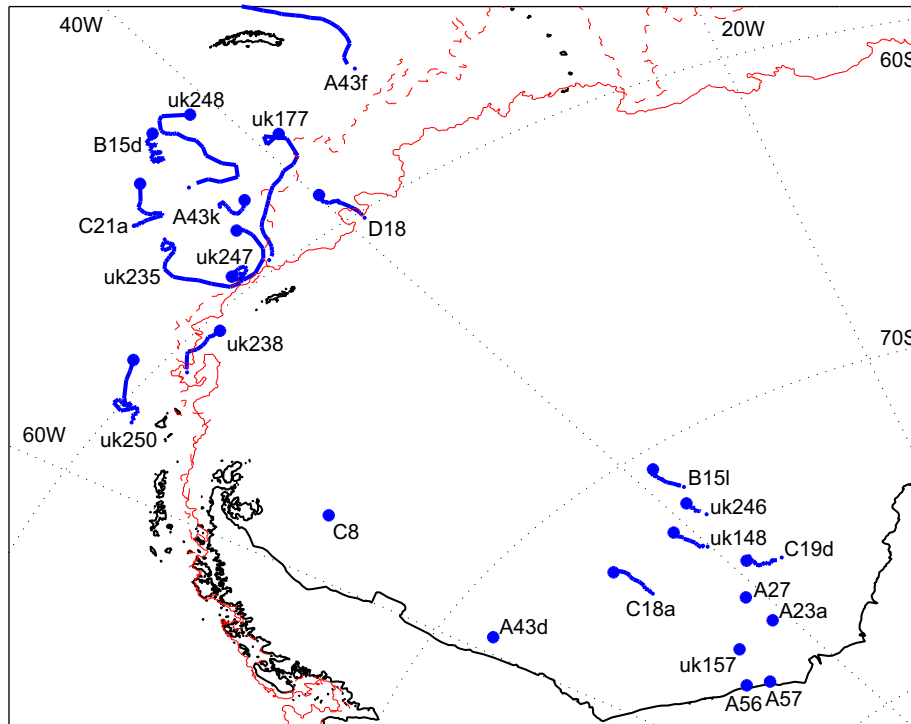


**Fig. 12.** Tracks of Antarctic icebergs and high-backscatter contacts detected using SeaWinds in the Weddell and Scotia Seas during the 2008 NSF Antarctica cruise. Final iceberg tracking positions are indicated with “\*”. The Antarctic peninsula and the Filchner–Ronne Ice Shelf are outlined at the bottom of the image. The sea-ice edge at the beginning and ending of the cruise is indicated by solid and dashed lines. See Table 4 for corresponding iceberg statistics.

support reliable iceberg tracking. As a result, the majority of updates provided during the 2008 cruise were based on 24-hour SIR images.

In addition to tracking iceberg positions in real-time, the sea-ice edge was annotated in the daily iceberg reports during the 2008 and 2009 NSF cruises. While auto-tracking the sea-ice edge from daily SeaWinds images is possible (Anderson and Long, 2005; Remund and Long, 1999; Haarpaintner et al., 2004), we manually tracked the edge in the NRT reports. As previously discussed, the sea-ice edge is visible in backscatter images as a region whose associated backscatter typically lies between low-backscatter sea water and high-backscatter icebergs, such as in Fig. 4. In the event of iceberg surface melting, the sea-ice edge can be differentiated between iceberg signatures with an iceberg tracking time-series, such as in Fig. 16B.

#### 3.4.3. The 2009 cruise

The third NSF Antarctic cruise took place in 2009, Julian days 68–101. During this time, most of the icebergs detected were in the Weddell Sea. Extensive sea ice recession, characteristic of the height of the austral ablation, allowed for close observation of these icebergs. Icebergs tracked during this mission are included in Table 5 with corresponding tracks in Fig. 13.

For the 2009 cruise, there were two iceberg position reporting methodologies. Initially, iceberg reports were relayed twice per day based upon the 24-hour SIR images developed for the 2008 cruise. However, in order to expand the search to icebergs in the Weddell Sea and gain an understanding of sea-ice extent and momentum, the boundaries of the 24-hour SIR images were expanded from 55–65°S and 60–40°W to 55–67°S and 60–25°W during the initial week of the cruise. Due to file size constraints, reports were reduced in frequency to once per day. This is the primary reason behind the lower number of iceberg updates reported in 2009 compared to 2005 and 2008 in Table 2. Using this methodology, the 2009 cruise successfully located icebergs C-18a (twice) and B-15l.

#### 3.4.4. Sample data

To facilitate close-proximity iceberg studies, backscatter images from SeaWinds and subsequently derived iceberg positions were transmitted to a surface ship in the Weddell and Scotia Seas during the 2005, 2008, and 2009 NSF Antarctic cruises. Examples of these periodic updates are included in Fig. 14. Fig. 14A emphasizes the Scotia Sea and was primarily used for the 2005 and 2008 cruise. Fig. 14B portrays the Scotia Sea and Weddell Sea during the 2009 cruise. The Antarctic peninsula land mass is outlined at the bottom-left of both images. The sea ice extent has been marked with hand-drawn lines. Notice how the glacial continent and icebergs have the greatest backscatter signatures, sea ice has a moderate radar return, and sea water is characterized by varying low  $\sigma^0$  values.

## 4. Discussion

Validating iceberg positions in the MERS Antarctic iceberg database is accomplished by correlating iceberg positions using high-resolution imagery from the NIC and other sources. An example of a SeaWinds backscatter image and collocated MODIS optical image reported by the NIC of iceberg C-19a is displayed in Fig. 15. Similarly, high-resolution images of iceberg A-22a are displayed in Fig. 16. Fig. 16A–D correspond to SeaWinds h-pol backscatter images on 2006 Julian day 110, 2006 Julian day 303, 2007 Julian day 064, and 2007 Julian day 152. Fig. 16E–H correspond to DMSP IR, MODIS, AVHRR, and optical photography from astronauts on the International Space Station (ISS) on the same days. Because the ISS photograph was shot with a hand-held camera at a highly oblique angle, iceberg dimensions in the photograph may be slightly exaggerated but we note the similarities in overall shape between the photograph and the corresponding SeaWinds image.

Iceberg A-22a is observed in Fig. 16A as the high-backscatter target in the center. A likely melt event between 2006 Julian day 110 and 303 likely changed the dielectric of the iceberg’s surface,

**Table 5**

Compilation of icebergs and high-backscatter targets detected by the SeaWinds scatterometer in the Weddell and Scotia Seas during the 2009 NSF Antarctica cruise. Lifetime and mission-specific statistics are illustrated for each contact including detection dates, position, average daily movement during the cruise, a flag indicating sea ice encapsulation during the cruise, and iceberg dimensions reported by the NIC. See Fig. 13 for corresponding track illustration. Icebergs visited during the cruise are indicated with “\*”.

Lifetime information				Cruise-Specific information (2009 JD 068–101)				
Name	Track dates	Initial pos. (° N, ° E)	Final pos. (° N, ° E)	Initial pos. (° N, ° E)	Final pos. (° N, ° E)	Avg. daily movement (km)	Sea ice	NIC size (nm)
A-23a	99JD202–09JD244	–76.27, –41.81	–76.05, –41.35	–76.11, –41.58	–76.11, –41.58	0.0	Y	40 × 32
A-27	99JD200–09JD244	–76.23, –43.33	–74.84, –39.88	–75.14, –41.63	–75.14, –41.44	1.4	Y	10 × 8
A-43d	01JD123–09JD244	–71.20, –58.70	–70.52, –58.08	–71.25, –58.26	–71.12, –57.45	3.4	Y	21 × 16
A-55	08JD258–09JD216	–65.73, –60.81	–63.60, –56.48	–65.13, –57.78	–64.55, –56.23	5.4	Y	14 × 4
A-56	08JD148–09JD244	–77.12, –50.12	–77.15, –49.94	–77.08, –49.89	–77.11, –49.87	2.5	Y	14 × 7
A-57	08JD151–09JD145	–77.40, –48.24	–77.60, –47.59	–77.54, –48.04	–77.46, –47.96	1.6	Y	19 × 5
B-151*	07JD054–09JD244	–66.48, 46.60	–62.06, –37.97	–65.44, –40.72	–65.43, –40.79	2.5	M	16 × 7
C-8	99JD202–09JD244	–67.30, 147.08	–60.87, –43.21	–60.80, –47.40	–61.59, –46.74	4.0	N	15 × 8
C-18a*	05JD152–09JD244	–65.20, 115.25	–59.92, –45.05	–62.40, –51.92	–61.78, –49.06	7.8	N	17 × 3
C-19d	03JD173–09JD244	–69.53, 163.30	–57.08, –49.17	–69.19, –52.29	–67.99, –53.06	6.7	Y	17 × 8
UK-157	07JD032–09JD244	–76.51, –46.70	–73.97, –42.52	–76.26, –43.13	–76.15, –42.80	3.4	Y	–
UK-247	08JD074–09JD103	–59.86, –47.90	–55.46, –35.52	–55.45, –35.54	–55.49, –35.72	4.2	N	–
UK-263	08JD228–09JD206	–74.46, –30.64	–68.48, –50.13	–72.82, –43.83	–72.01, –44.98	6.9	Y	–
UK-276	08JD334–09JD244	–65.92, –60.95	–65.42, –60.73	–65.81, –60.73	–65.55, –60.70	3.2	Y	–
UK-284	09JD046–09JD244	–63.50, –51.44	–60.95, –43.70	–63.26, –50.01	–62.11, –50.24	7.4	N	–
UK-285	09JD027–09JD138	–64.09, –53.70	–61.70, –49.52	–63.67, –51.70	–62.47, –51.59	7.8	N	–
TK-230	09JD064–09JD099	–64.05, –54.93	–64.19, –54.76	–64.15, –54.74	–64.19, –54.76	3.9	N	–
TK-231	09JD070–09JD116	–63.92, –53.98	–63.54, –51.21	–63.92, –53.98	–63.89, –51.34	8.0	N	–
TK-232	09JD060–09JD099	–64.79, –55.51	–64.49, –53.86	–64.99, –55.01	–64.49, –53.86	7.0	M	–
TK-233	09JD070–09JD075	–66.07, –50.93	–66.06, –49.65	–66.07, –50.93	–66.06, –49.65	15.5	N	–
TK-234	09JD071–09JD090	–65.65, –38.77	–65.87, –38.88	–65.65, –38.77	–65.87, –38.88	6.0	N	–
TK-235	09JD073–09JD096	–63.68, –51.90	–63.67, –51.14	–63.68, –51.90	–63.67, –51.14	8.0	N	–
TK-236	09JD073–09JD084	–65.36, –55.79	–65.21, –56.28	–65.36, –55.79	–65.21, –56.28	10.1	N	–
TK-237	09JD073–09JD082	–66.05, –50.97	–65.89, –50.89	–66.05, –50.97	–65.89, –50.89	10.2	N	–
TK-238	09JD076–09JD089	–66.80, –46.21	–66.78, –46.91	–66.80, –46.21	–66.78, –46.91	6.8	N	–

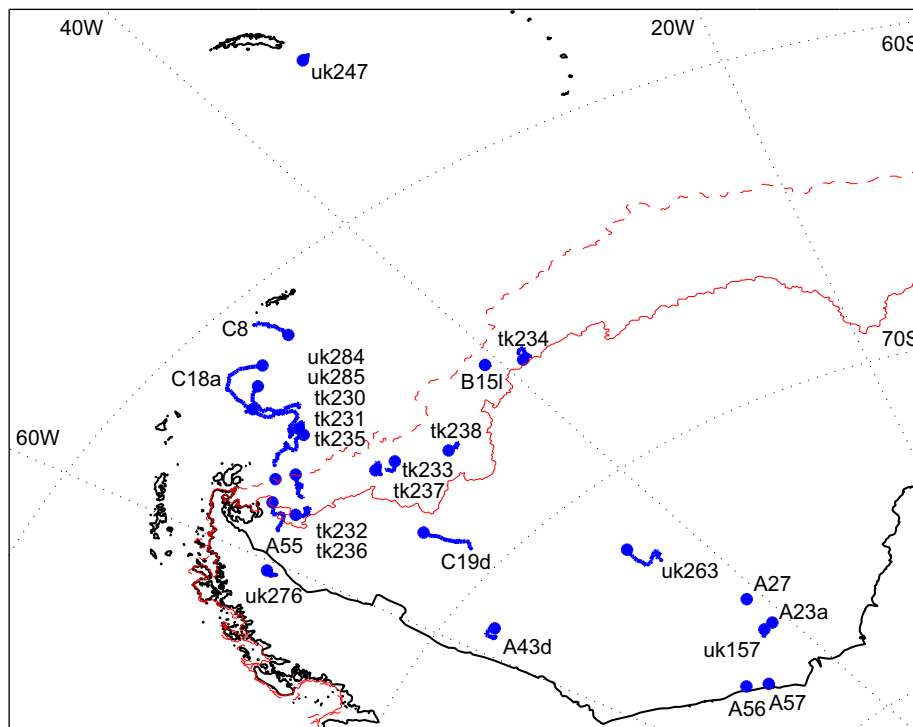


**Fig. 13.** Tracks of Antarctic icebergs and high-backscatter contacts detected using SeaWinds in the Weddell and Scotia Seas during the 2009 NSF Antarctica cruise. Final iceberg tracking positions are indicated with “\*”. The Antarctic peninsula and the Filchner–Ronne Ice Shelf are outlined at the bottom of the image. The sea-ice edge at the beginning and ending of the cruise is indicated by solid and dashed lines. See Table 5 for corresponding iceberg statistics.

reducing backscatter and causing iceberg A-22a to appear as bright as nearby sea ice in Fig. 16B. Fig. 16F gives a higher-resolution look of the nearby sea ice. Similarly, the backscatter reduction in Fig. 16C

is likely caused by surface melt. In Fig. 16D, melt conditions have abated and the high-backscatter profile of iceberg A-22a is observed once more.

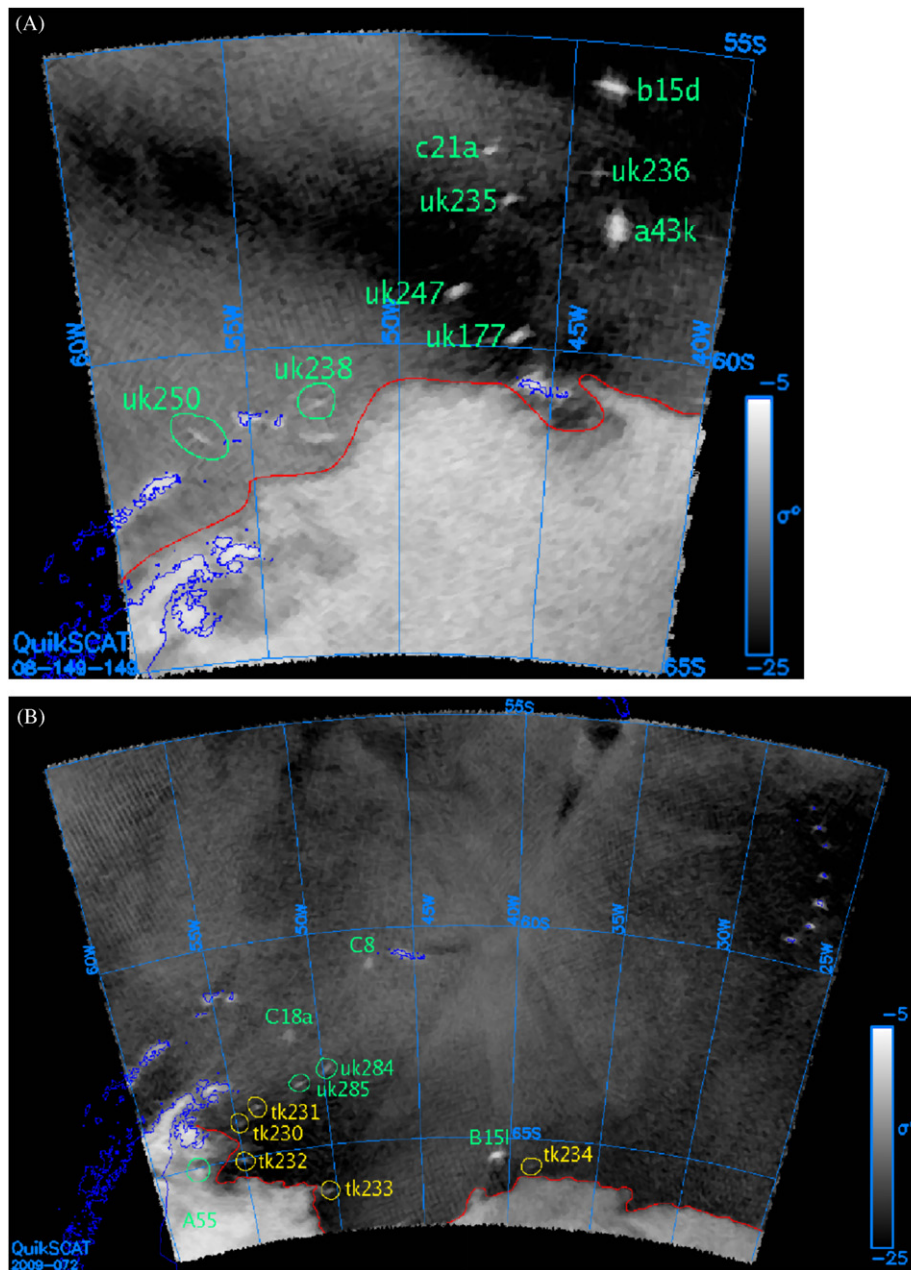


**Fig. 14.** Custom 24-hour SIR images created from SeaWinds h-pol backscatter measurements for the NSF Antarctic cruises. These images were included in iceberg position reports during the NSF Antarctic cruises on (A) 2008 Julian day 149 and (B) 2009 Julian day 72. High, medium, and low-backscatter regions are characteristic of glacial ice, sea ice, and sea water, respectively. The positions of Antarctic icebergs and temporary contacts are labeled. The Antarctic peninsula land mass is outlined in both images at the bottom-left of both images. Sea ice extent is also indicated with hand-drawn lines.

As mentioned in Section 2.5.2, during periods of rapid iceberg movement, a time delay between when SeaWinds radar measurements are collected and when iceberg positions are analyzed and reported may result in discrepancies between the reported and the actual iceberg positions. During the NSF cruises, this delay ranged between 12 and 30 h, resulting in iceberg position discrepancies up to 25 km. Because ocean currents are the dominant factor influencing free-floating iceberg movement (Guily, 1988; Schodlok et al., 2006), NRT iceberg movement was compensated for by analyzing nearby and recent iceberg movement patterns. Iceberg locations were estimated given the last known iceberg position and velocity to enable ship interception and navigation.

Noted that even though cruise logistics and sea-ice proximity limited the close-proximity research to only a select few icebergs,

tracking all nearby contacts, including “TK” contacts, proved to be helpful in subjectively determining ocean current speed and direction for estimating future iceberg positions.

Even though SeaWinds was never designed to track icebergs, our results demonstrate the utility of using SeaWinds measurements in developing an iceberg position database and in tracking icebergs in real-time. Knowledge of iceberg position is important for safety reasons and for modeling geophysical processes such as surface freshwater sources (Stephenson et al., 2011). Iceberg positions have been validated by using collocated high-resolution satellite imagery and by navigating cruise ships to physically intercept several large tabular icebergs in the Weddell and Scotia Seas during three NSF Antarctic cruises (Smith, 2011). Due to low costs, other scatterometers can also be used to reliably track icebergs in the future.

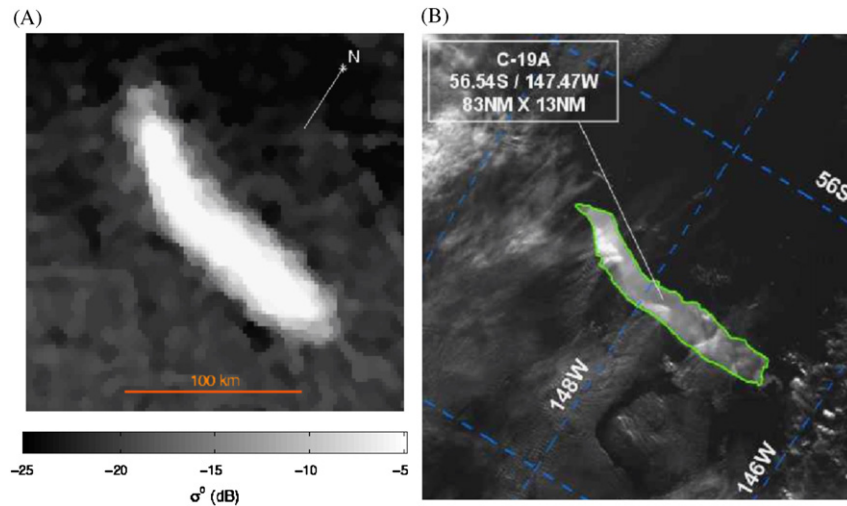


**Fig. 15.** Images of iceberg C-19a on 2008 Julian day 170 from (A) the SeaWinds scatterometer and (B) MODIS (an optical imager). Annotation in (B) performed by the NIC.

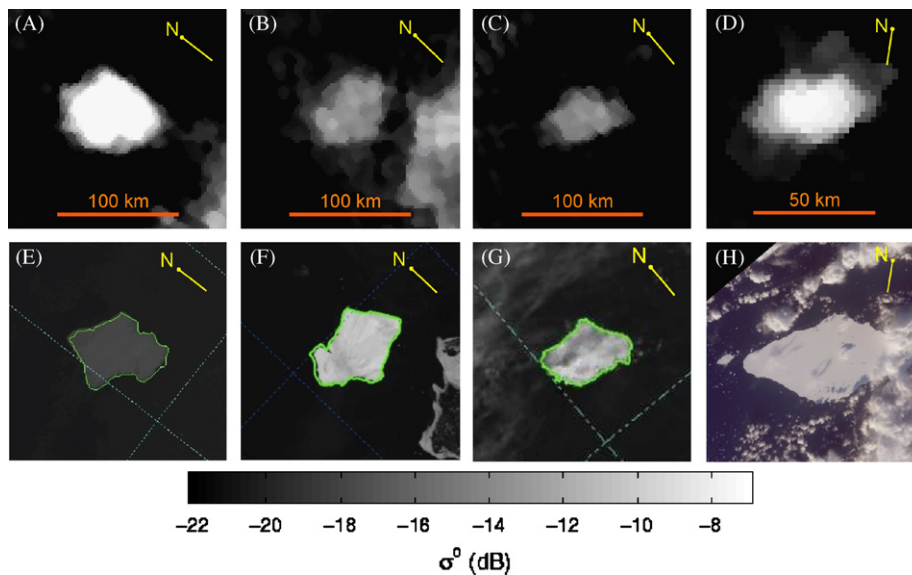


**Fig. 16.** Images of iceberg A-22a from the SeaWinds scatterometer and other high-resolution sensors. Fig. 16A–D correspond to SeaWinds h-pol backscatter SIR images on 2006 Julian day 110, 2006 Julian day 303, 2007 Julian day 64, and 2007 Julian day 152. Fig. 16E–H correspond to a DMSP IR image on 2006 Julian day 110, a MODIS image on 2006 Julian day 303, an AVHRR image on 2007 Julian day 64, and an optical photograph taken by astronauts on the ISS on 2007 Julian day 152 (compliments of NASA). The bright area at the right of (B) is due to the sea-ice edge. (B) and (C) appear darker than (A) and (D) due to surface melt conditions on these days. The colorbar at the bottom corresponds to (A–D). Annotation in (E–G) performed by the NIC. (E–G) were obtained from the NIC. (H) was obtained from NASA.

## Acknowledgments

We thank the National Science Foundation for their support of the 2005, 2008, and 2009 Antarctic cruises. We also thank the officers, crew, and scientists aboard the first cruise ARSV L.M. Gould cruise LMG05-014A and the second and third cruises RVIB N.B. Palmer, NBP08-06 and NBP09-02, for their hard work at sea. This research was funded in part by the National Science Foundation under contract ANT-0636440. We also thank the NIC for providing high-resolution imagery of icebergs in the Southern Ocean.

## References

- Anderson, H.S., Long, D.G., 2005. Sea ice mapping method for SeaWinds. IEEE Transactions on Geoscience and Remote Sensing 43 (3), 647–657.
- Ashcraft, I.S., Long, D.G., 2003. The spatial response function of SeaWinds backscatter measurements. In: Proceedings of SPIE, vol. 5151, Earth Observing Systems VIII, August 2003, pp. 609–618.
- Ballantyne, J., 2002. A multidecadal study of the number of Antarctic icebergs using scatterometer data. Technical Report, Brigham Young University online report: (<http://www.scp.byu.edu/data/iceberg/IcebergReport.pdf>).
- Bindschadler, R.A., Rignot, E., 2001. “Crack” in the polar night. EOS, Transactions, American Geophysical Union 82, 497–505.
- Drinkwater, M.R., Long, D.G., Bingham, A.W., 2001. Greenland snow accumulation estimates from satellite radar scatterometer data. Journal of Geophysical Research 106 (D24), 33935–33950.
- Early, D.S., Long, D.G., 2001. Image reconstruction and enhanced resolution imaging from irregular samples. IEEE Transactions on Geoscience and Remote Sensing 39 (2), 291–302.
- Forester, R.R., Long, D.G., Jezek, K.C., Drobot, S.D., Anderson, M.R., 2001. The onset of Arctic sea-ice snowmelt as detected with passive- and active-microwave remote sensing. Annals of Glaciology 33, 85–93.
- Guily, B.S., 1988. The drift of icebergs under wind action. Journal of Geophysical Research 93 (C4), 3608–3612.
- Haarpaintner, J., Tonboe, R.T., Long, D.G., van Woert, M.L., 2004. Automatic detection and validity of the sea-ice edge: an application of enhanced-resolution QuikScat/SeaWinds data. IEEE Transactions on Geoscience and Remote Sensing 42 (7), 1433–1443.
- Haykin, S., Lewis, E.O., Raney, R.K., Rossiter, J.R., 1994. Remote Sensing of Sea Ice and Icebergs. John Wiley & Sons, Inc.

- Kristensen, M., 1983. Iceberg calving and deterioration in Antarctica. *Progress Physical Geography* 7, 313–328.
- Kunz, L.B., Long, D.G., 2004. Melt detection in Antarctic ice-sheets using spaceborne scatterometers and radiometers. *IEEE Transactions on Geoscience and Remote Sensing* 1, 117–120.
- Lazzara, M.A., Jezek, K.C., Scambos, T.A., MacAyeal, D.R., van der Veen, C.J., 1999. On the recent calving of icebergs from the Ross ice shelf. *Polar Geography* 23, 201–212.
- Long, D.G., Collyer, R.S., Reed, R., Arnold, D.V., 1996. Dependence of the normalized radar cross section of water waves on Bragg wavelength–wind speed sensitivity. *IEEE Transactions on Geoscience and Remote Sensing* 34 (3), 656–666.
- Long, D.G., Hardin, P., Whiting, P., 1993. Resolution enhancement of spaceborne scatterometer data. *IEEE Transactions on Geoscience and Remote Sensing* 31 (3), 700–715.
- Long, D.G., Spencer, M.W., 1997. Radar backscatter measurement accuracy for a spaceborne pencil-beam wind scatterometer with transmit modulation. *IEEE Transactions on Geoscience and Remote Sensing* 35 (1), 102–114.
- MacAyeal, D.R., Okal, M.H., Thom, J.E., Brunt, K.M., Kim, Y., Bliss, A.K., 2008. Tabular iceberg collisions within the coastal regime. *Journal of Glaciology* 54 (185), 371–386.
- Massom, R., 1991. *Satellite Remote Sensing of Polar Regions*. Lewis Publishers.
- Naderi, F.M., Freilich, M.H., Long, D.G., 1991. Spaceborne radar measurement of wind velocity over the ocean—an overview of the NSCAT scatterometer system, vol. 79, pp. 850–866.
- NIC, update 2010. National Ice Center. <<http://www.natice.noaa.gov/>>.
- Remund, Q.P., Long, D.G., 1999. Sea ice mapping using ku band scatterometer data. *Journal of Geophysical Research* 104 (C5), 11515–11527.
- Scambos, T.A., Hulbe, C., Fahnestock, M., Bohlander, J., 2000. The link between climate warming and break-up of ice shelves in the Antarctic peninsula. *Journal of Glaciology* 46, 516–530.
- Scambos, T., Sergienko, O., Sargent, A., MacAyeal, D., Fastook, J., 2005. ICES at profiles of tabular iceberg margins and iceberg breakup at low latitudes. *Geophysical Research Letters* 32. doi:10.1029/2005GL023802.
- Schodlok, M.P., Hellmer, H.H., Rohardt, G., Fahrbach, E., 2006. Weddell Sea iceberg drift: five years of observations. *Journal of Geophysical Research* 111. doi:10.1029/2004JC002661.
- SCP, update 2010. Scatterometer Climate Record Pathfinder. <<http://www.scp.byu.edu/>>.
- Sharma, N., D'Sa, E., 2008. Assessment and analysis of QuikSCAT vector wind products for the Gulf of Mexico: a long-term and hurricane analysis. *Sensors* 8 (3), 1927–1949.
- Smith Jr, K.L., 2011. Free-drifting icebergs in the Southern Ocean: an overview. *Deep-Sea Research II* 58 (11–12), 1277–1284.
- Spencer, M.W., Long, D.G., 2000. Improved resolution backscatter measurements with the SeaWinds pencil-beam scatterometer. *IEEE Transactions on Geoscience and Remote Sensing* 38 (1), 89–104.
- Spencer, M.W., Wu, C., Long, D.G., 1997. Tradeoffs in the design of a spaceborne scanning pencil beam scatterometer: application to SeaWinds. *IEEE Transactions on Geoscience and Remote Sensing* 35 (1), 115–126.
- Stephen, H., Long, D.G., 2000. Study of iceberg B10A using scatterometer data. In: *Proceedings of the International Geoscience and Remote Sensing Symposium*, vol. 3. Honolulu, HI, pp. 1340–1342.
- Stephenson Jr, G.R., Sprintall, J., Gille, S.T., Vernet, M., Helly, J.J., Kaufmann, R.S., 2011. Subsurface melting of a free-floating Antarctic iceberg. *Deep-Sea Research II* 58 (11–12), 1336–1345.
- Tournadre, J., Whitmer, K., Girard-Arduin, F., 2008. Iceberg detection in open water by altimeter waveform analysis. *Journal of Geophysical Research—Oceans* 113 (August). doi:10.1029/2007JC004587.
- Ulaby, F.T., Moore, R.K., Fung, A.K., 1981. *Microwave Remote Sensing*, vol. 1. Addison-Wesley.
- Zwally, H.J., Comiso, J.C., Parkinson, C.L., Cavalieri, D.J., Gloersen, P., 2002. Variability of Antarctic sea ice 1979–1998. *Journal of Geophysical Research* 107 (C5). doi:10.1029/2000JC000733.